Supporting Information for:

High Rate Sodium Ion Battery Anodes from Block Copolymer Templated Mesoporous Nickel- Cobalt Carbonates and Oxides

Sarang M. Bhaway, Pattarasai Tangvijitsakul, Jeongwoo Lee, Mark D. Soucek, Bryan D. Vogt[*]

Department of Polymer Engineering, University of Akron, Akron OH 44325
*Address correspondence to vogt@uakron.edu
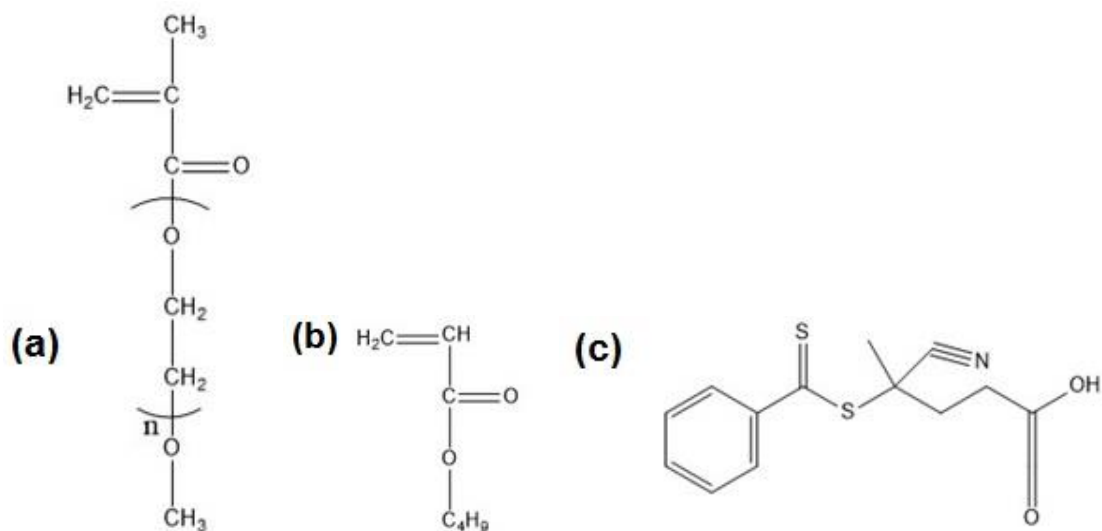
Figure S1. Chemical structures of the monomers used for the synthesis: (a) Methoxy poly(ethylene glycol) methacrylate (n = 11, MPEGMA 475) and (b) Butyl acrylate (BA). (c) 4-cyanopentanoic acid dithiobenzoate (CPADB) is used as the RAFT agent.
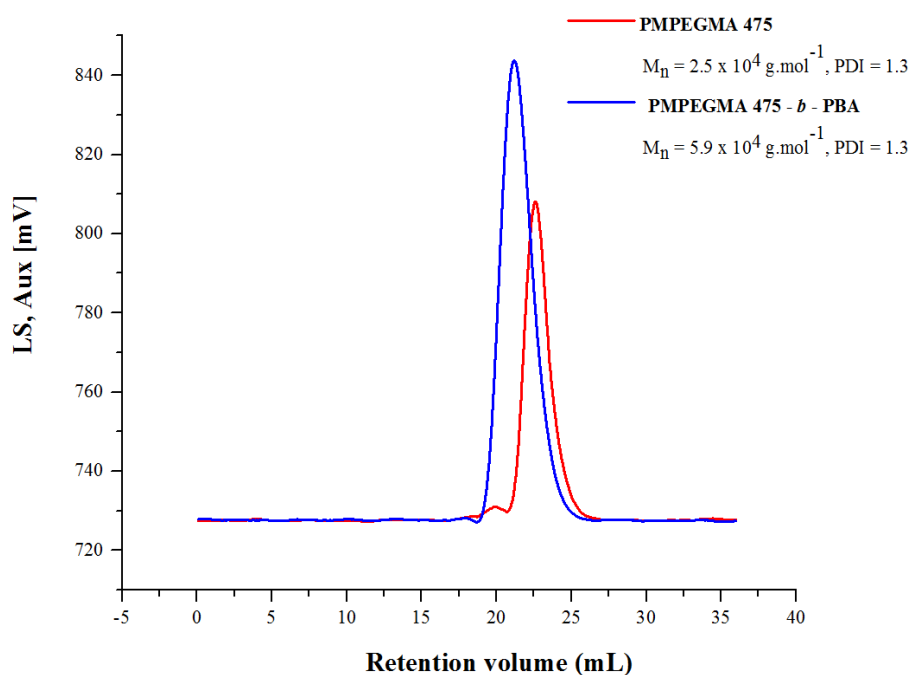
Figure S2. GPC chromatogram (THF as a solvent) of RAFT poly (MPEGMA) and RAFT poly (MPEGMA) − *b* − PBA. The molecular weight was determined using PS standards.
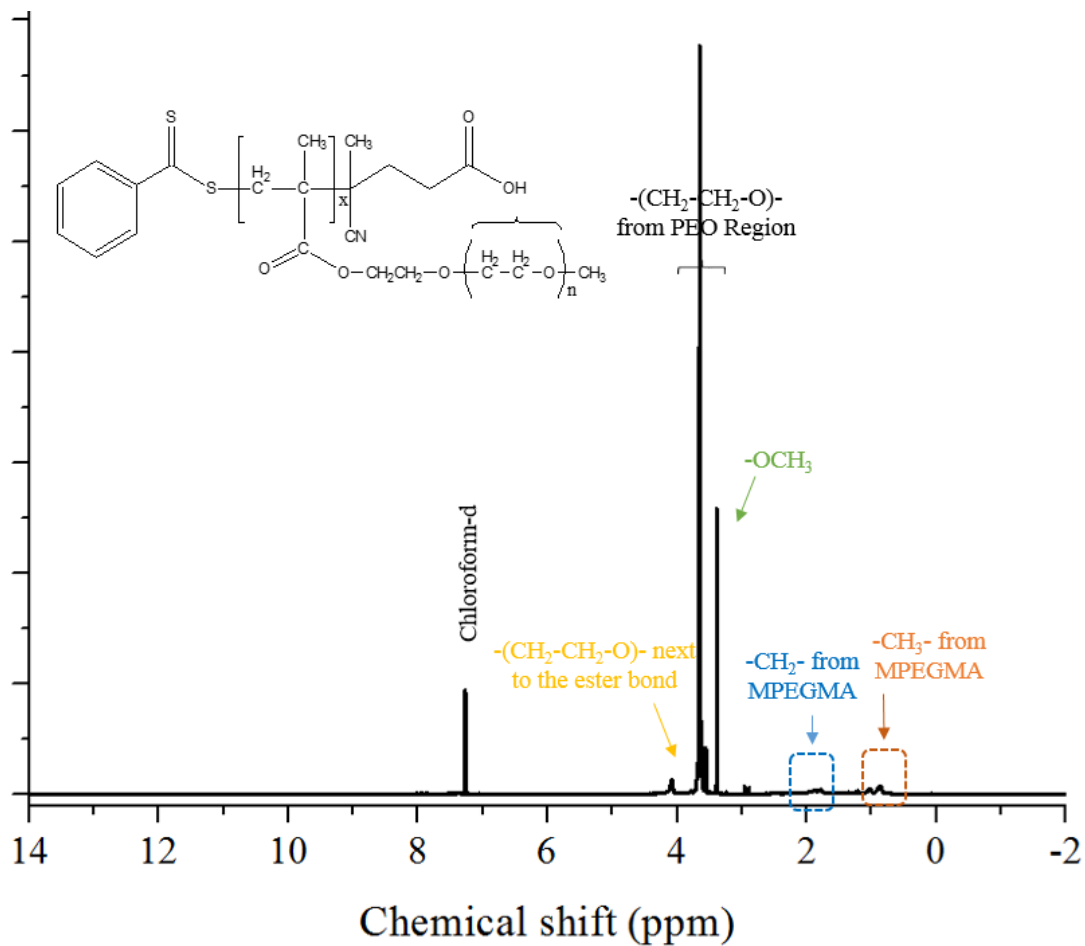
Figure S3. ^{1}H-NMR of RAFT poly (MPEGMA).

Table S1. [1]H resonance assignments of RAFT poly (MPEGMA)

Structural Group	Chemical Shift (ppm)
-CH$_2$-CCH$_3$ (main chain)	0.88 - 1.11
-CH$_2$-CCH$_3$ (main chain)	1.58 - 2.04
-O-CH$_3$	3.39
-(CH$_2$CH$_2$O)- (PEO region)	3.42 - 3.80
-OCO-(CH$_2$CH$_2$O)-	3.98 - 4.08
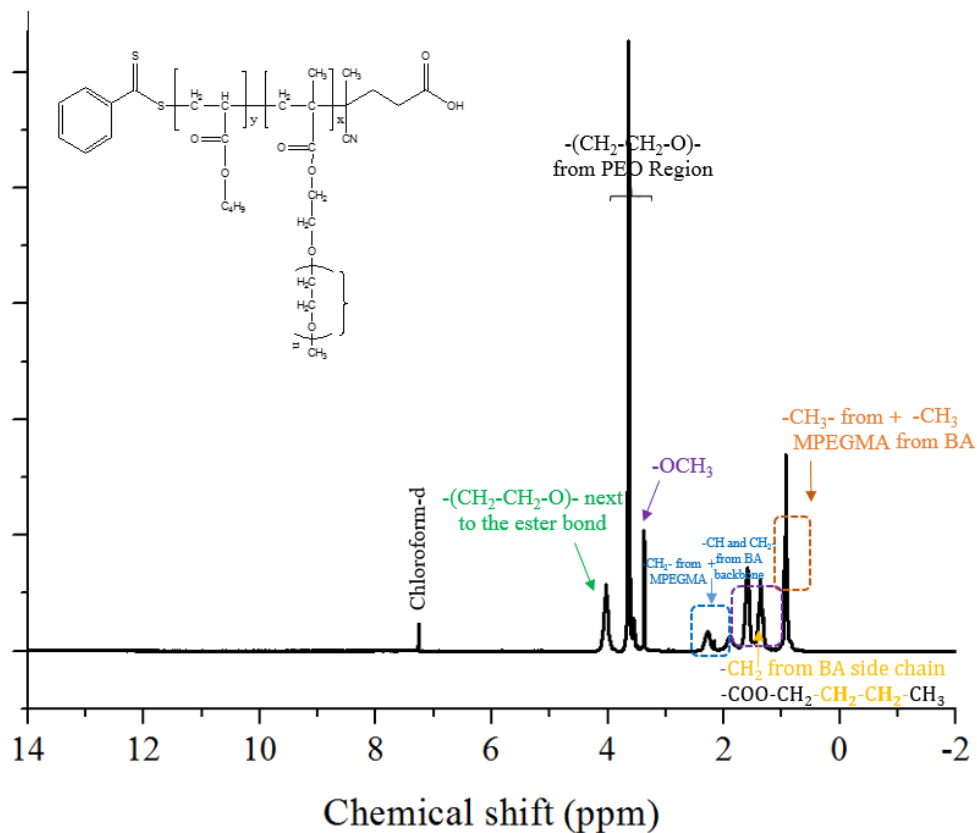
Figure S4. ^{1}H-NMR of RAFT poly (MPEGMA) – *b* – PBA

Table S2. [1]H resonance assignments of RAFT poly (MPEGMA) – *b* - PBA

Structural Group	Chemical Shift (ppm)
-CH$_2$-CC<u>H</u>$_3$ (MPEGMA) and −O-CH$_2$-CH$_2$-CH$_2$-C<u>H</u>$_3$ (BA)	0.80-1.10
-COO-CH$_2$-CH$_2$-C<u>H</u>$_2$-CH$_3$ (BA)	1.35 - 1.37
-COO-CH$_2$-C<u>H</u>$_2$-CH$_2$-CH$_3$ (BA)	1.57 - 1.62
-C<u>H</u>$_2$-CCH$_3$ (MPEGMA) and -C<u>H</u>$_2$-C<u>H</u>- (BA)	1.89 - 2.30
-O-C<u>H</u>$_3$	3.39
-(C<u>H</u>$_2$C<u>H</u>$_2$O)- (PEO region)	3.54 - 3.78
-COO-(C<u>H</u>$_2$C<u>H</u>$_2$O)- (MPEGMA) and -COO-C<u>H</u>$_2$-CH$_2$-CH$_2$-CH$_3$ (BA)	3.97 - 4.15
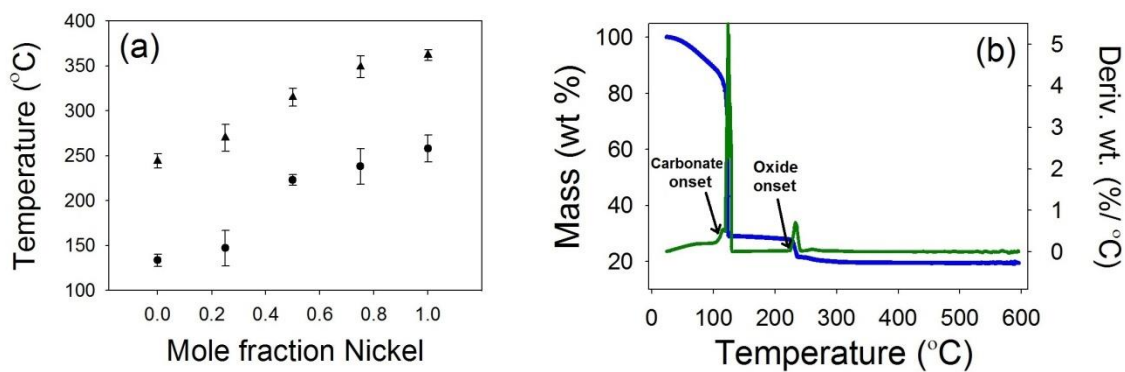
Figure S5. (a) Onset temperature for formation of metal carbonate (circle) and metal oxide (triangle) with varying nickel content within the composite determined from TGA traces. (b) TGA trace (blue) and derivative (green) of mass loss for cobalt nitrate-citric acid complex, indicating two step degradation corresponding to formation of cobalt carbonate followed by decomposition of carbonate into cobalt oxide
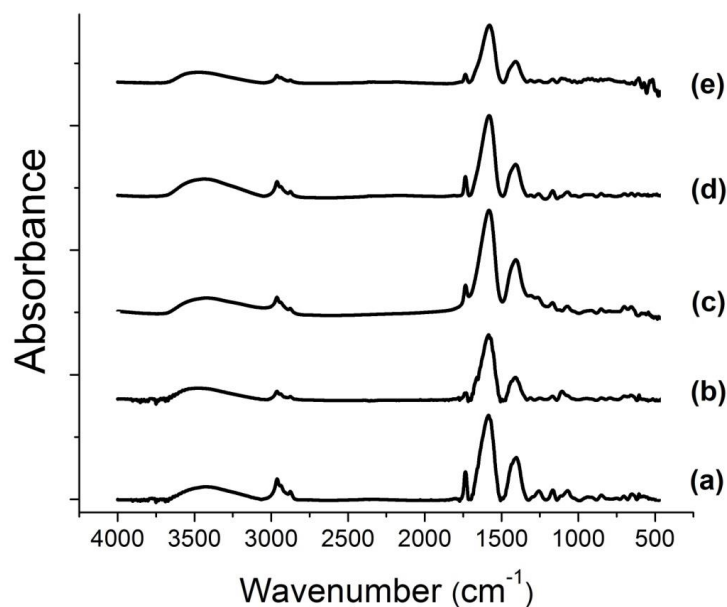
Figure S6. FTIR spectra of block copolymer micelle templated (a) $Co(CO_3)_y$ (b) $NiCo_2(CO_3)_y$ (c) $Ni_{1.5}Co_{1.5}(CO_3)_y$ (d) $Ni_2Co(CO_3)_y$ (e) $Ni(CO_3)_y$
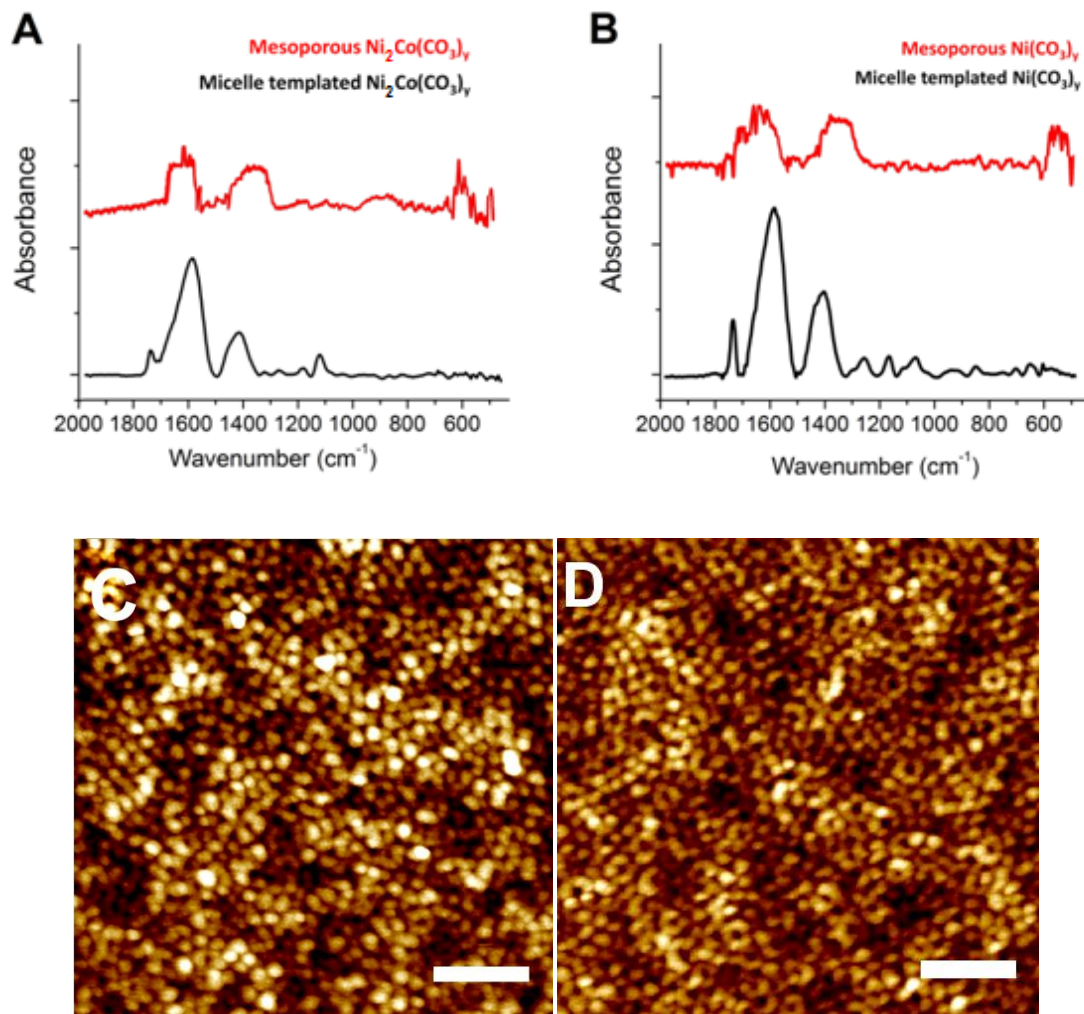
Figure S7. FTIR spectra tracking the removal of PMPEGMA-*b*-PBA block copolymer template from thin films of (A) Ni$_2$Co(CO$_3$)$_y$ and (B) Ni(CO$_3$)$_y$. AFM micrographs indicating an ordered mesoporous structure for (C) Ni$_2$Co(CO$_3$)$_y$ and (D) Ni(CO$_3$)$_y$. (Scale bar = 200 nm)
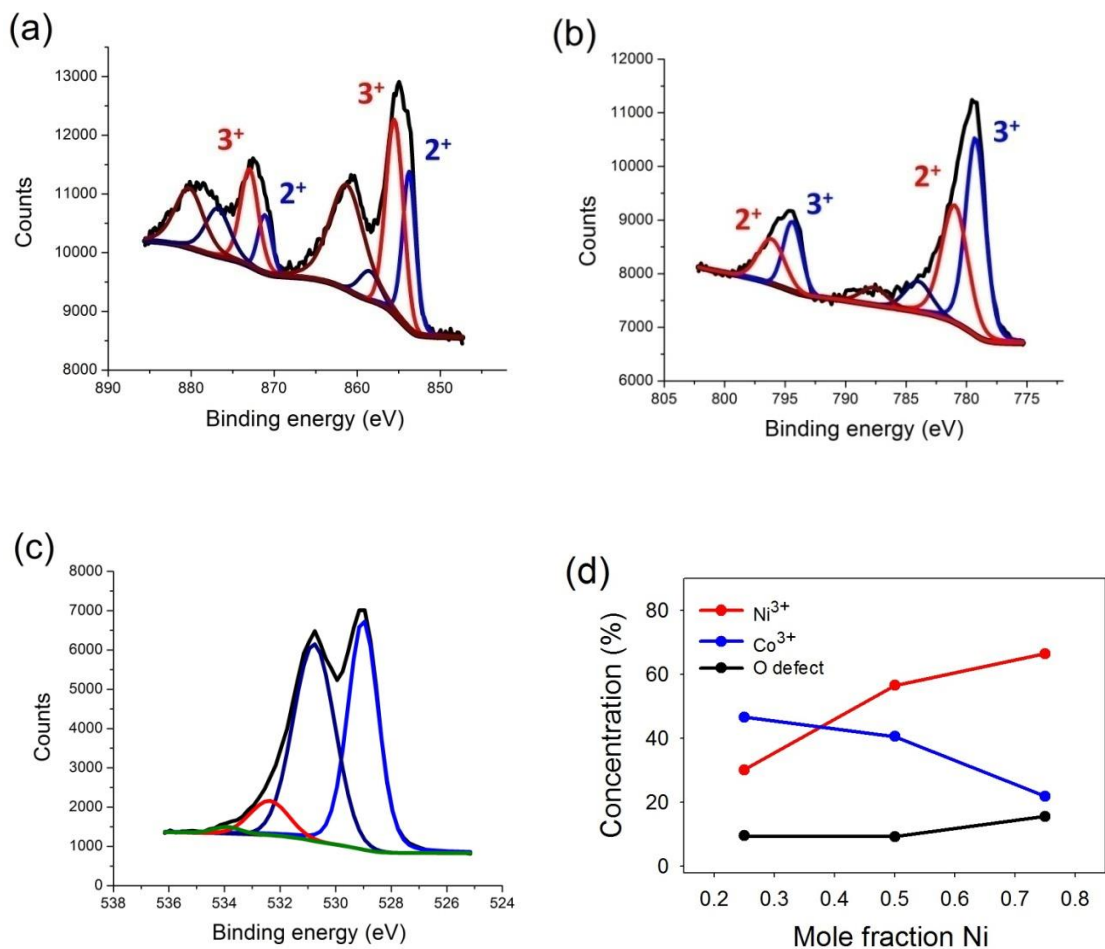
Figure S8. High resolution XPS profiles of (a) Ni2p (b) Co2p and (c) O1s peaks present in templated mesoporous $Ni_{1.5}Co_{1.5}O_4$ thin film. Ni and Co are found to be present as a mixture of 2^+ and 3^+ oxidation state in the MMO composite. (d) Variation in atomic % of Ni (red), Co (blue) and defect O concentration (black) in the MMO with varying nickel content

To further characterize the chemical composition of the mesoporous composites, x-ray photoelectron spectroscopy (XPS) was performed on the MMO thin films. Figure S8 illustrates the high resolution scans for Ni2p and Co2p regions along with O1s region for $Ni_{1.5}Co_{1.5}O_4$. As can be seen in Figure S8(a), the Ni2p spectra is composed to two spin-orbit doublets corresponding to 2 different oxidation states (Ni^{3+} and Ni^{2+}) along with 2 satellite peaks corresponding to each oxidation state within the $Ni_{1.5}Co_{1.5}O_4$.[1, 2] Quantitative analysis of Ni2p peak indicates 55.4 % population of Ni^{3+} oxidation state within the porous MMO. Similarly, the Co2p spectrum also exhibits two spin-orbit doublets indicating cobalt to be present as Co^{3+} (41.5 %) and Co^{2+} (58.8 %) within $Ni_{1.5}Co_{1.5}O_4$. The O1s spectra on the other hand, can be deconvoluted into 4 distinct peaks with peak positions centered around 528.8 eV, 530.6 eV, 532 eV and 533.3 eV. Each of these peaks corresponds to oxygen bound in different environment, namely oxygen-metal bond, oxygen present in the hydroxyl group, defect oxygen sites within the MMO and physisorbed or chemisorbed water molecules on the thin film surface. The atomic ratio of (Ni:Co:O) determined from XPS analysis indicates a ratio of $(1.72 : 1.53 : 4)$, which quite close to the theoretical chemical composition predicated for $Ni_{1.5}Co_{1.5}O_4$.

From Figure S8(d), we can see that the population of Ni^{3+} monotonically increases, while Co^{3+} population decreases with increase in nickel content within the MMO. At the same time, the defect oxygen concentration in the MMO also increases with increase in nickel content within the

MMO composite. When additional nickel is added to the nickel-cobalt composite, Ni^{2+} ions begin to occupy the Co lattice sites, where Co^{3+} was initially present in the MMO. This leads to deficiency of positive charges and to maintain charge neutrality, Ni^{2+} transforms to Ni^{3+}.[3] As a result, the Ni^{3+} population is found to increase while Co^{3+} decreases with increasing nickel content within the MMO. The increase in oxygen defect concentration with nickel content again indicates intercalation of nickel within the cobalt lattice and formation of a MMO crystal structure.[3]
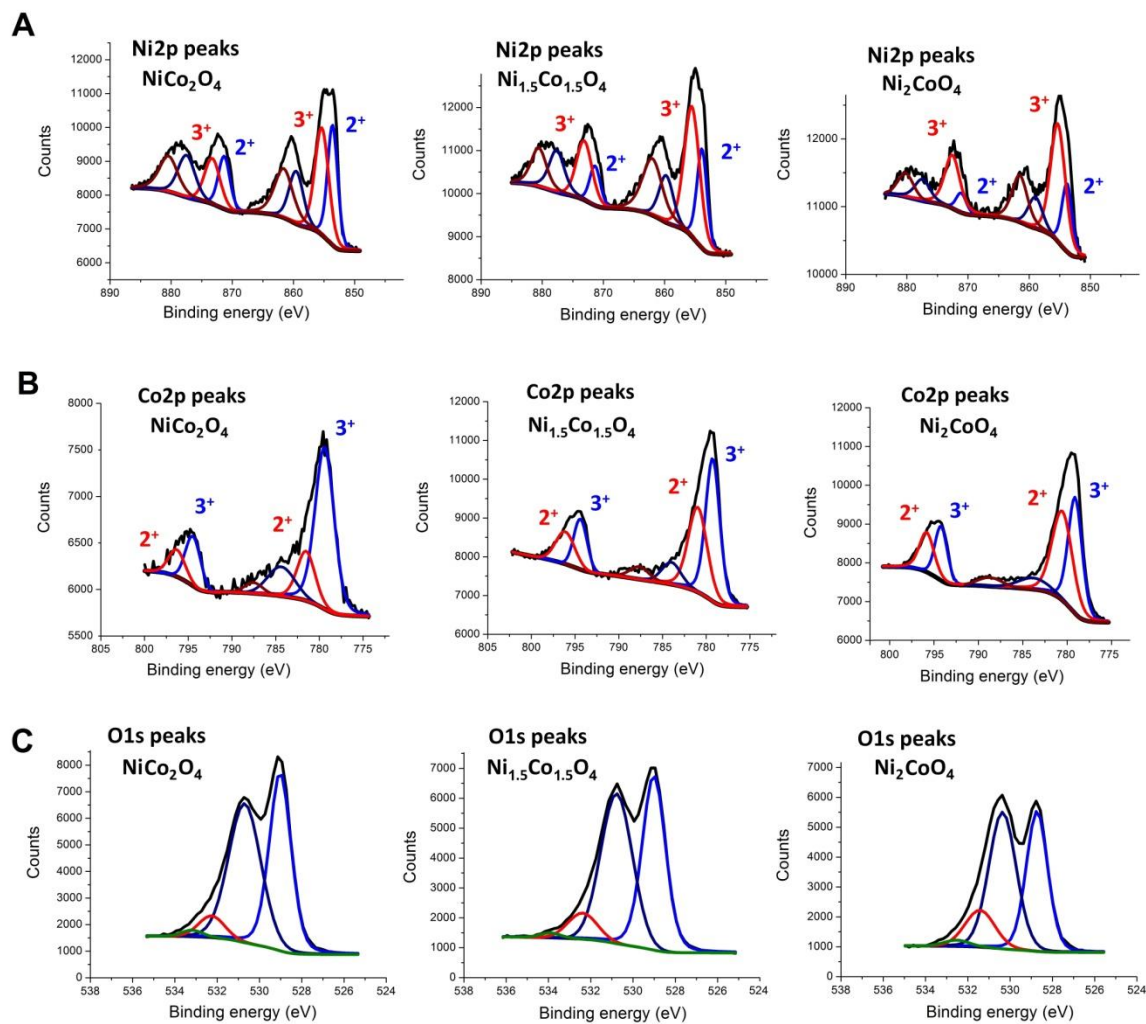
Figure S9. High resolution XPS profiles of (A) Ni2p (B) Co2p and (C) O1s peaks present in templated mesoporous $Ni_xCo_{(3-x)}O_4$ thin films along with deconvolution of peaks indicating Ni and Co to be present as a mixture of oxidation states in the MMO composite.
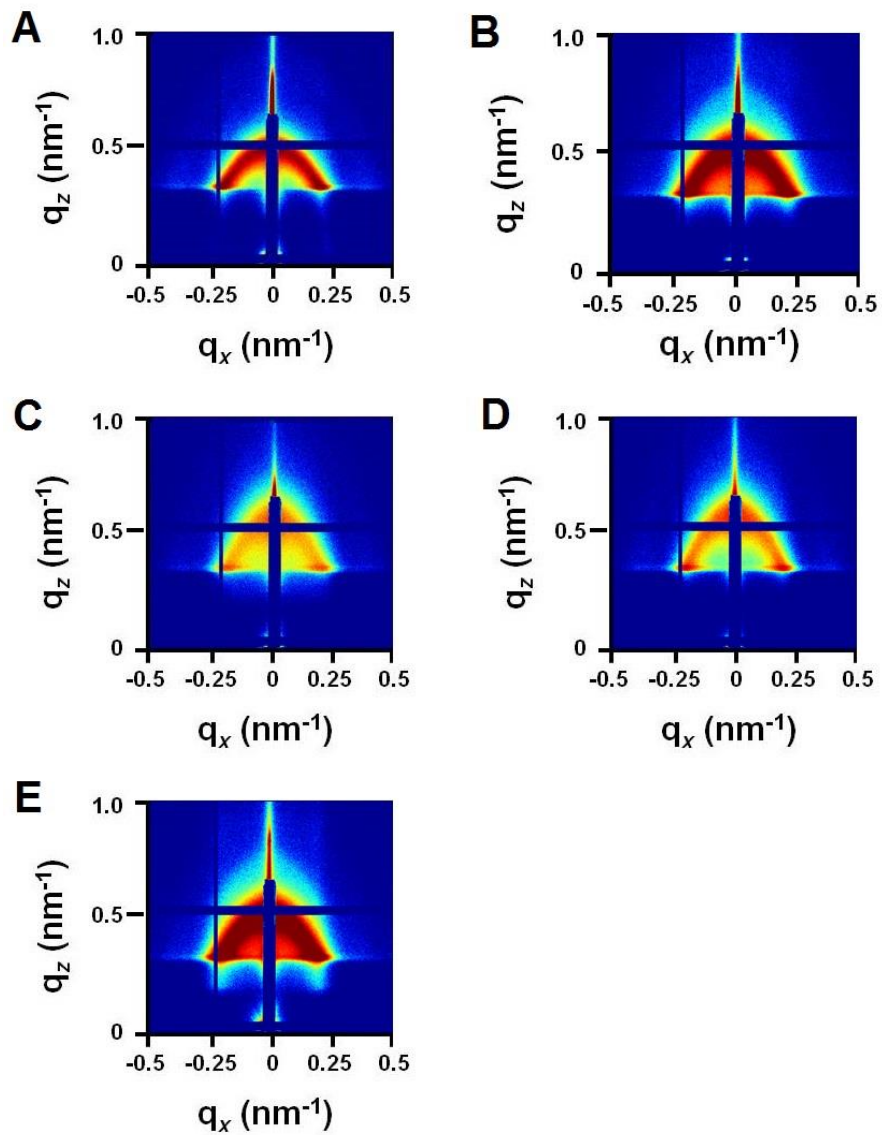
Figure S10. 2-D GISAXS profiles of micelle templated (A) $Co(CO_3)_y$ (B) $NiCo_2(CO_3)_y$ (C) $Ni_{1.5}Co_{1.5}(CO_3)_y$ (D) $Ni_2Co(CO_3)_y$ (E) $Ni(CO_3)_y$ at incident angle of 0.2°, illustrating the ellipsoidal patterns arising from cubic mesostructure.
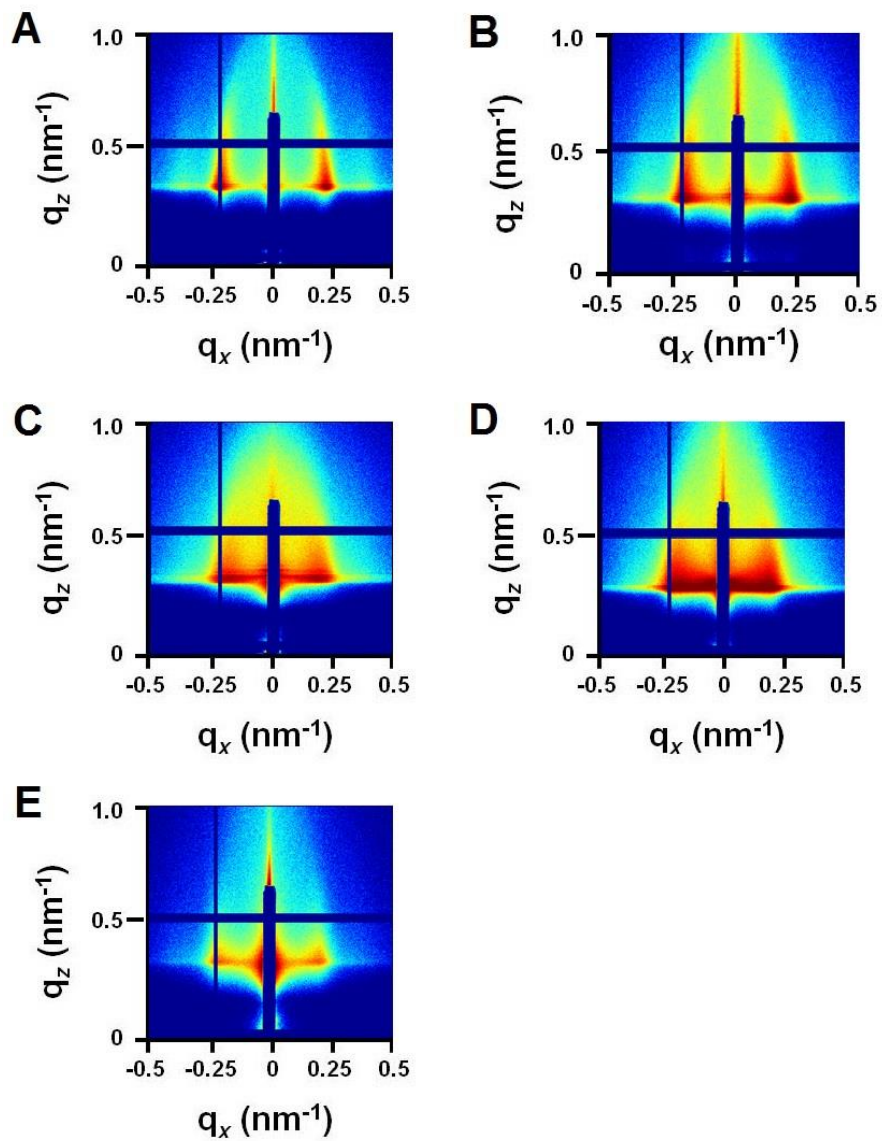
Figure S11. 2-D GISAXS profiles of ordered mesoporous (A) Co_3O_4 (B) $NiCo_2O_4$ (C) $Ni_{1.5}Co_{1.5}O_4$ (D) Ni_2CoO_4 (E) NiO at incident angle of 0.2°, illustrating that the ordered structure is maintained after template removal and decomposition of metal carbonate to corresponding oxide.
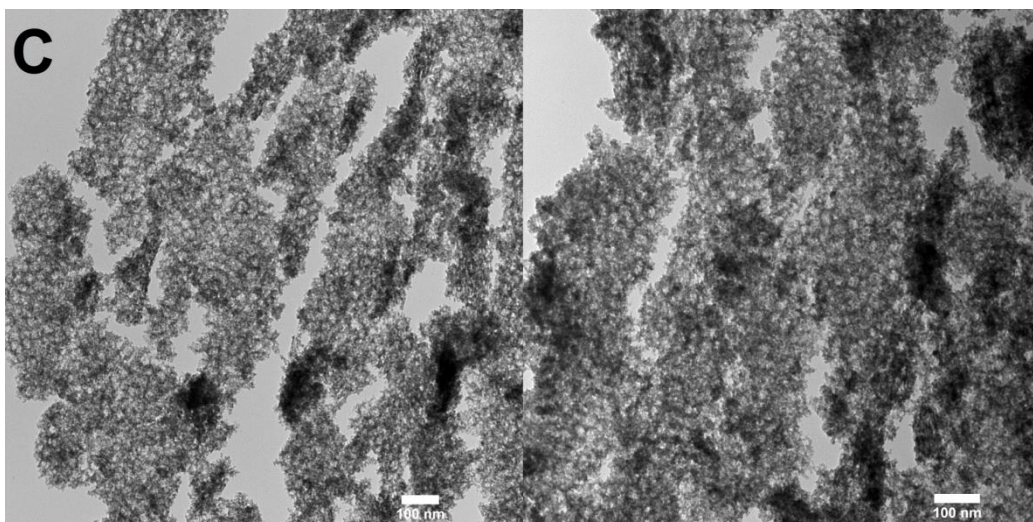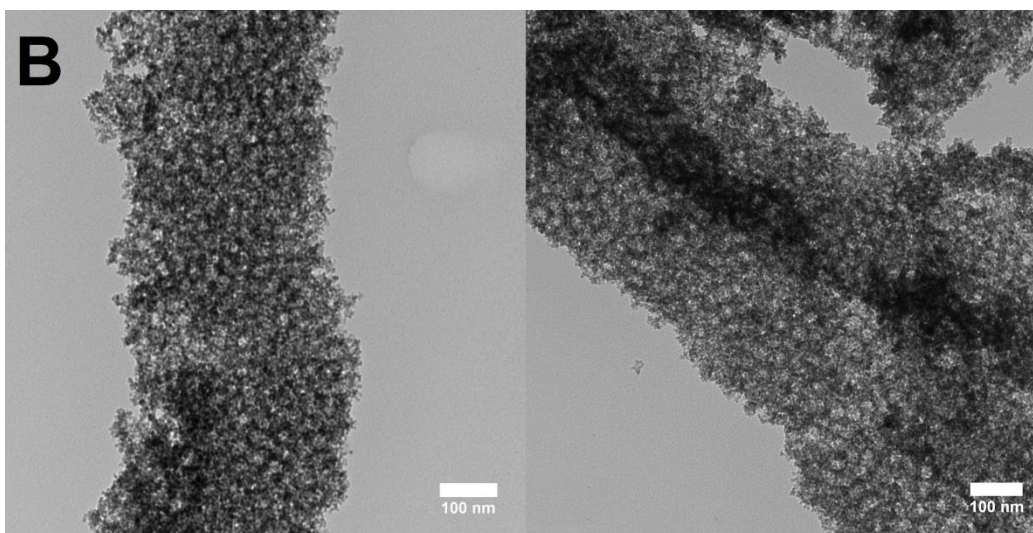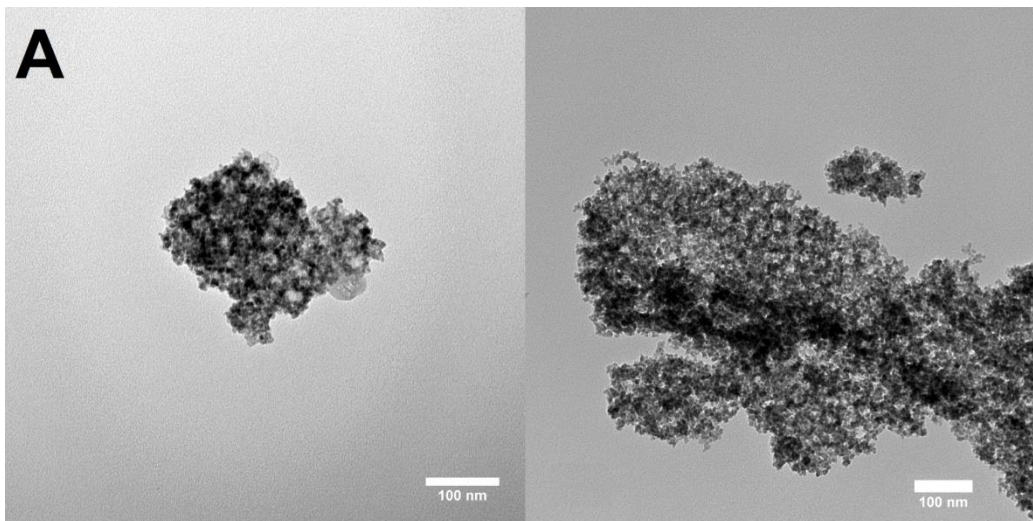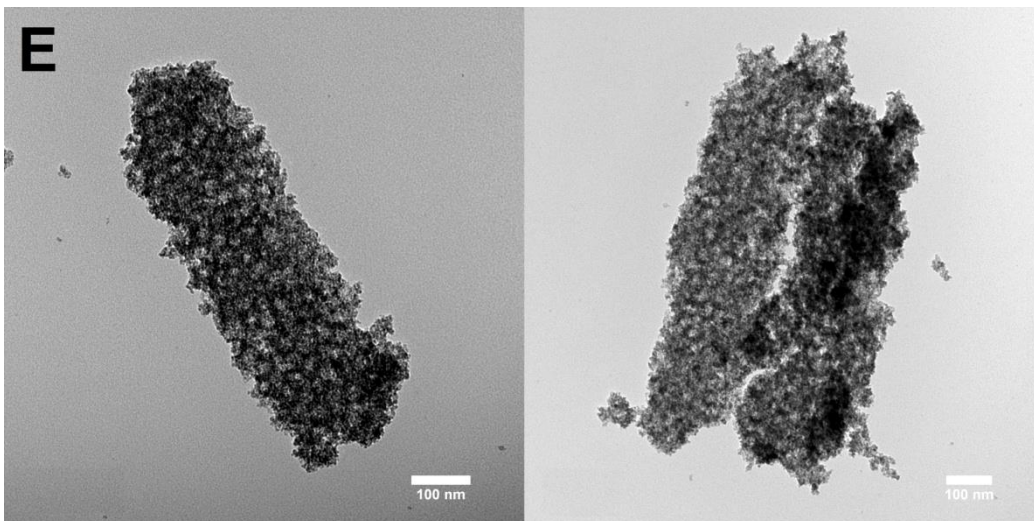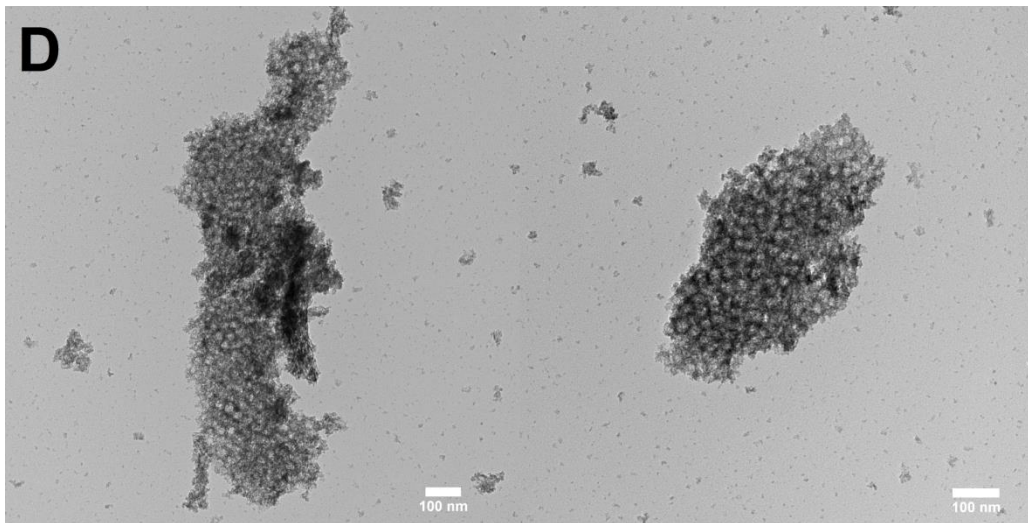
Figure S12. TEM micrographs of samples prepared from scrapped films of (A) Co_3O_4 (B) $NiCo_2O_4$ (C) $Ni_{1.5}Co_{1.5}O_4$ (D) Ni_2CoO_4 and (E) NiO. Ordered mesoporous structure with spherical pores (~ 14 nm) can be clearly seen in all the oxide film samples (Scale bar=100 nm)
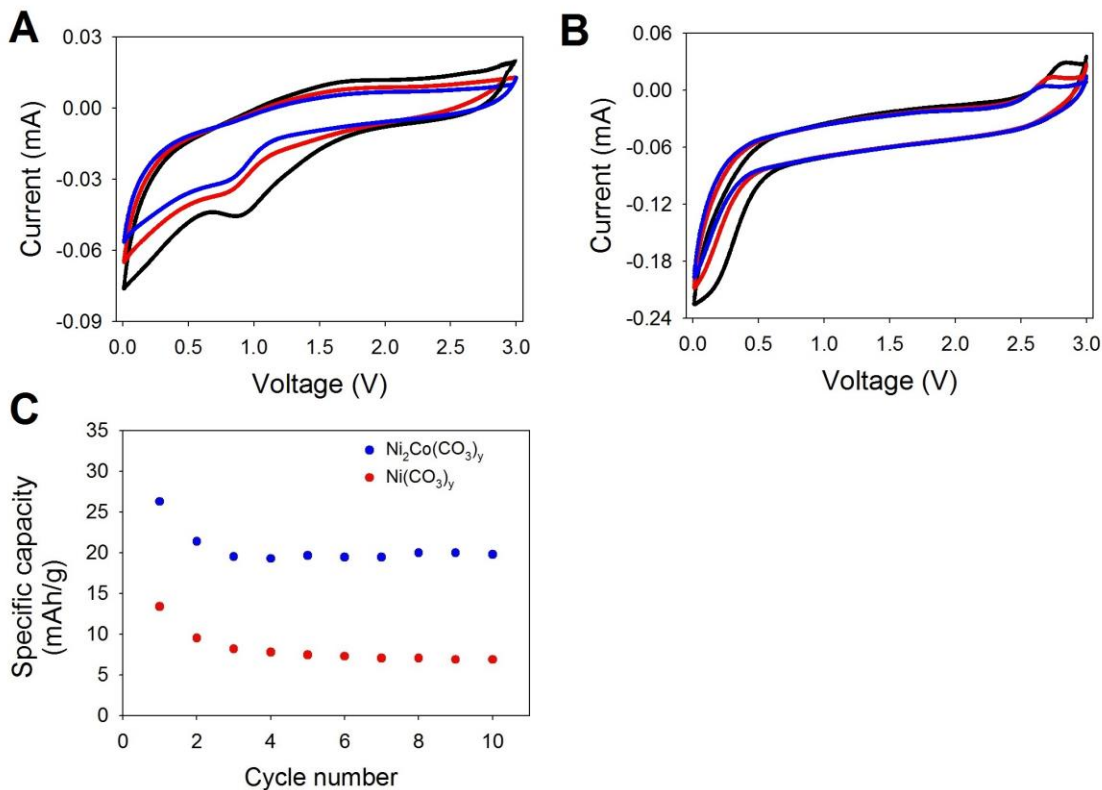
Figure S13. Cyclic voltammetry curves of (A) $Ni_2Co(CO_3)_y$ and (B) $Ni(CO_3)_y$ carried out at a scan rate of 2 mV/s. (C) Specific discharge capacity of mesoporous $Ni_2Co(CO_3)_y$ (●) and $Ni(CO_3)_y$ (▲) galvanostatically cycled at a constant current density of 1 A/g over voltage range 0.01- 3.0 V.

Few reports on use of mixed-metal carbonate based anodes have shown to provide high specific capacity and good cycling stability when used in lithium ion battery.[4-6] To test the impact of porosity on charge storage performance , mesoporous thin films of $Ni_2Co(CO_3)_y$ and $Ni(CO_3)_y$ were tested as sodium ion battery anodes at high current density of 1 A/g (Figure S13). Based on the CV curves (Figure S13A), mesoporous $Ni_2Co(CO_3)_y$ exhibits a broad cathodic reduction peak centered around 0.9 V due to metal carbonate reduction. Previous reports on use of manganese carbonate[7] and cobalt carbonate[8] anodes in lithium ion battery indicate formation of reduced metal and Li_2CO_3 during the cathodic reduction process. This reduced metal acts as an electrocatalyst facilitating further reduction of Li_2CO_3 to Li_2O along with formation of low valence carbon, which leads to enhanced specific capacity through faradic contributions.[8] We can expect a similar charge storage mechanism in case of $Ni_2Co(CO_3)_y$ anode when used in sodium ion battery, where reduction of $Ni_2Co(CO_3)_y$ to metallic Ni and Co occurs around 0.9 V (cathodic peak) followed by reduction of Na_2CO_3 to Na_2O. During the oxidation process, anodic peak is formed at 1.65 V. However, intensity of this anodic peak in successive cycles significantly reduces, which suggests irreversible sodium de-insertion from the $Ni_2Co(CO_3)_y$ matrix. On galvanostatically cycling the mesoporous $Ni_2Co(CO_3)_y$ at 1 A/g, the anode provides a low initial discharge capacity of 27 mAh/g (116 mAh/cm^3) with the value levelling off around 20 mAh/g (88 mAh/cm^3) at the end of 10 cycles (Figure S13C).

In case of mesoporous $Ni(CO_3)_y$, peak at low potential (~0.01-0.25 V) can be ascribed to electrolyte decomposition. However, no obvious redox peaks are visible in the CV curve indicating a capacitor-like behaviour with little or no sodium ion intercalation in the $Ni(CO_3)_y$ matrix. As the CV curves indicate limited reduction of $Ni(CO_3)_y$ to metallic Ni, the amount of electrocatalyst available to reduce Na_2CO_3 to Na_2O is lowered, which leads to overall decrease in specific capacity and inferior charge storage performance. Mesoporous $Ni(CO_3)_y$ anode on galvanostatic cycling at

1 A/g exhibits much inferior charge storage providing an initial discharge capacity of 14 mAh/g (98 mAh/cm^3) with poor cycling stability on further cycling. Thus, the poor charge storage performance of $Ni_2Co(CO_3)_y$ and $Ni(CO_3)_y$ anode can be ascribed to the limited reduction of metal carbonate to corresponding metal at high current densities, along with irreversible Na^+ ions de-insertion from the inorganic walls. The high current density (1 A/g) used can further prevent effective intercalation of Na^+ within the inorganic walls and hinder formation of a stable solid electrolyte interface (SEI), leading to overall inferior charge storage performance in the carbonates.
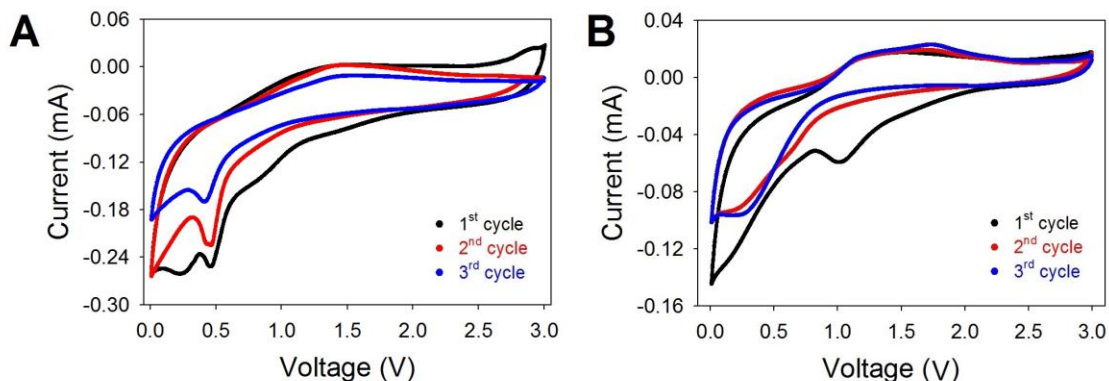
Figure S14. Cyclic voltammetry curves for (A) Co_3O_4 (B) NiO carried out at a scan rate 2 mV/s in the voltage range of 0.01-3.0 V.
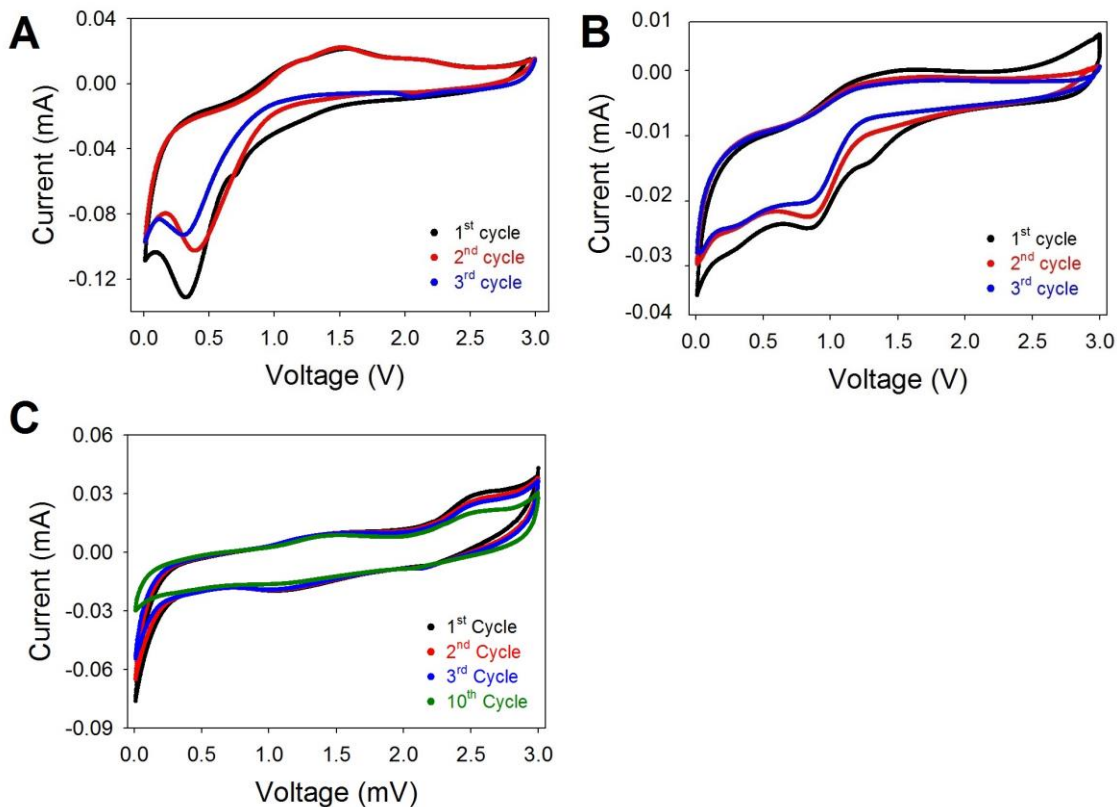
Figure S15. Cyclic voltammetry curves for (A) $NiCo_2O_4$ (B) $Ni_{1.5}Co_{1.5}O_4$ and (C) Ni_2CoO_4 carried out at a scan rate of 2 mV/s in the voltage range of 0.01-3.0 V

In case of $NiCo_2O_4$, a broad cathodic peak centered around 0.35 V is observed corresponding to partial reduction of Ni^{3+}, Ni^{2+}, Co^{3+} and Co^{2+} to metallic Ni and Co respectively, in the first cycle. (Figure S15 (A)). The small peak at 0.7 V can be assigned to electrochemical formation of Na_2O, irreversible SEI formation along with slight destruction of crystal structure in the first cycle. In the subsequent cycles, the cathodic peak shifts slightly to higher potential due to polarization effect of the anode in the first cycle.[9] The redox peaks observed at 1.5 V and 2.1 V in the anodic curve correspond to oxidation of Ni and Co to higher oxidation states of Ni^{2+} and Co^{2+} respectively. As can be seen in Figure S15, the intensity of cathodic peaks relative to the first cycle also drops significantly in the third cycle. This decrease in cathodic peak intensity matches with the poor cycling performance observed in case of $NiCo_2O_4$ anode subjected to galvanostatic cycling at 1 A/g (Figure 7). In case of $Ni_{1.5}Co_{1.5}O_4$, a similar trend is observed with the cathodic peaks occurring at a slightly higher voltage of 0.85 V (Figure S15B). Similar to $NiCo_2O_4$, intensity of cathodic peaks in $Ni_{1.5}Co_{1.5}O_4$ drop in subsequent cycles due to irreversible reactions and SEI formation. As can be seen in Figure S15C, mesoporous Ni_2CoO_4 anode exhibits an irreversible cathodic peak in the first few cycles at low voltage range (~0.01-0.25 V) due to electrolyte decomposition. At the same time, a broad cathodic reduction peak is observed at 1.1 V. In the subsequent cycles, the CV curves are found to almost overlap indicating the significantly enhanced cycling capability of Ni_2CoO_4 thin film anode. This matches with the galvanostatic cycling measurements (Figure 7) which demonstrates the excellent reversible cycling behaviour of Ni_2CoO_4 thin film anode.
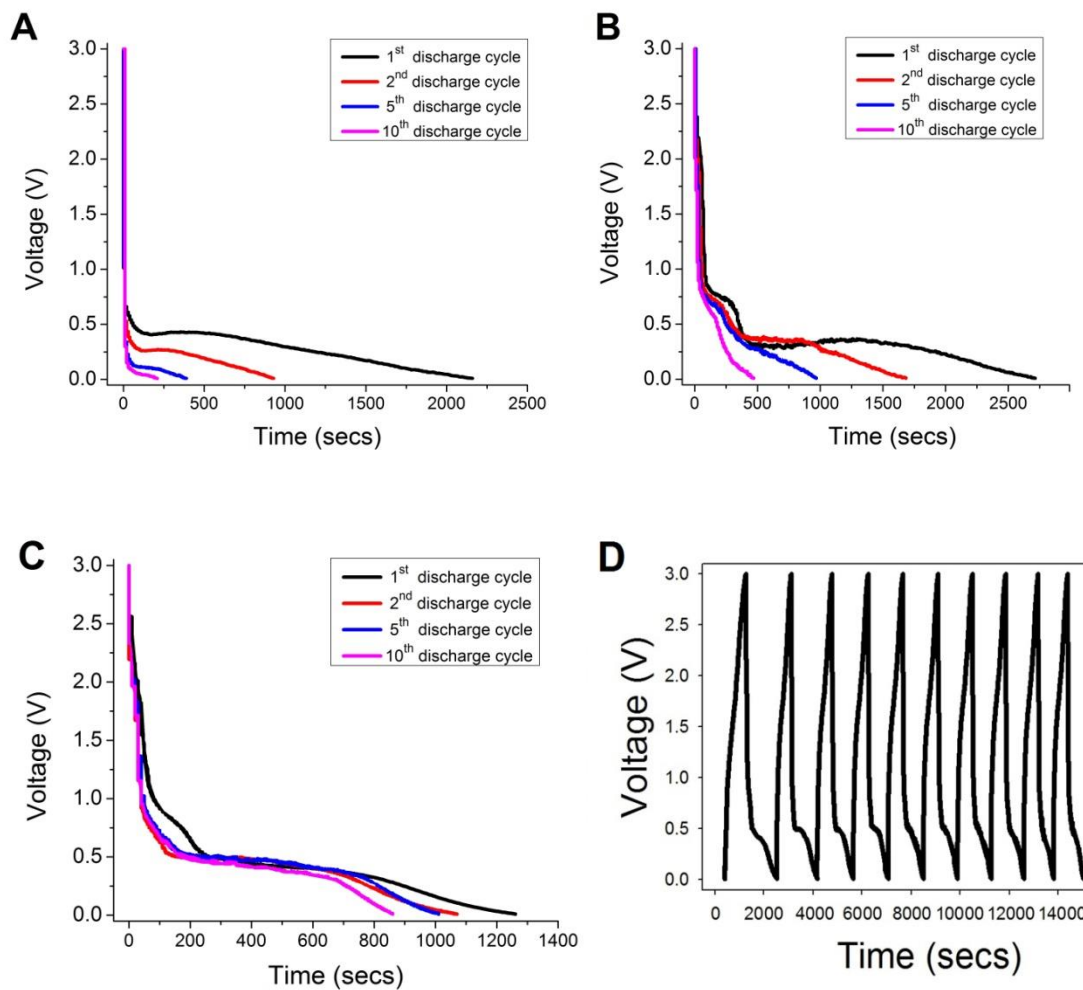
Figure S16. Galvanostatic discharge curves for (A) Co_3O_4 (B) NiO and (C) Ni_2CoO_4 indicating enhanced capacity retention over 10 cycles for Ni_2CoO_4 as compared to pure metal oxides. (D) Galvanostatic charge-discharge curves for Ni_2CoO_4 subjected to a constant current density of 1 A/g over voltage range 0.01- 3.0 V.
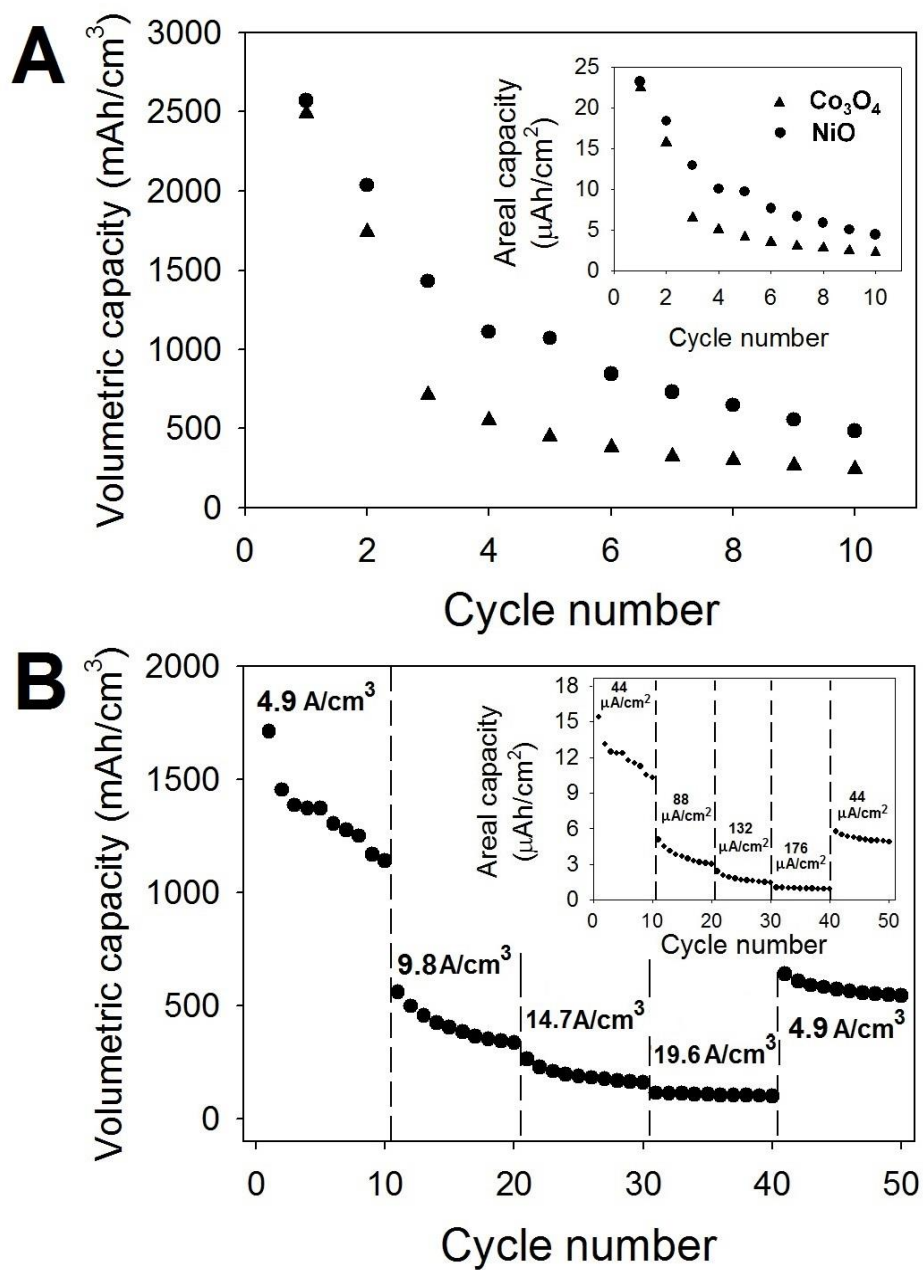
Figure S17. (A) Volumetric and areal discharge discharge capacity of mesoporous Co_3O_4 (▲) and NiO (●) thin film anodes galvanostatically cycled at a constant current density of approximately 4.15 A/cm^3 over voltage range of 0.01-3.0 V. (B) Cycling stability of mesoporous Ni_2CoO_4 subjected to galvanostatic cycling at varying volumetric and areal current densities.
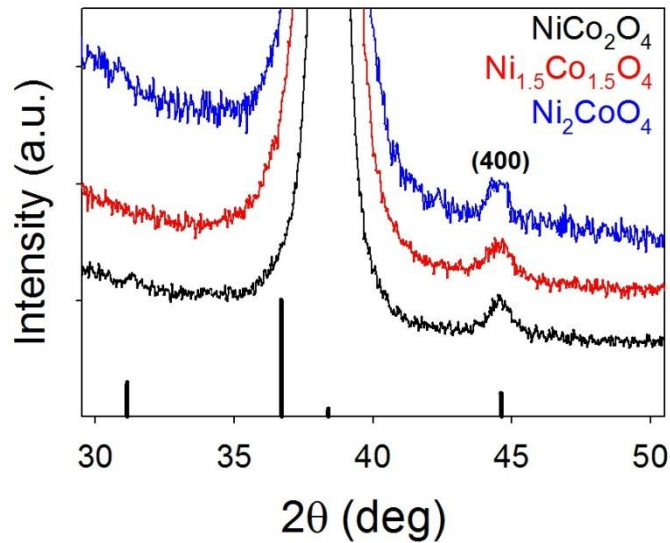
Figure S18. X-ray diffraction profiles of MMO thin film anodes subjected to galvanostatic cycling. The diffraction peak centered around 44.5° arises due to (400) crystal plane indicating that the crystal structure of the MMO is not destroyed following multiple insertion-deinsertion of Na^+ ions in the thin film anodes. The broad and intense peak centered at 38° arises due to gold sputtered on the quartz substrate, making it difficult to identify the space group of the MMO. The reference crystal planes indicated by the black lines correspond to *Fd-3m* spinel phase of $NiCo_2O_4$ (PDF card no. 01-073-1702).
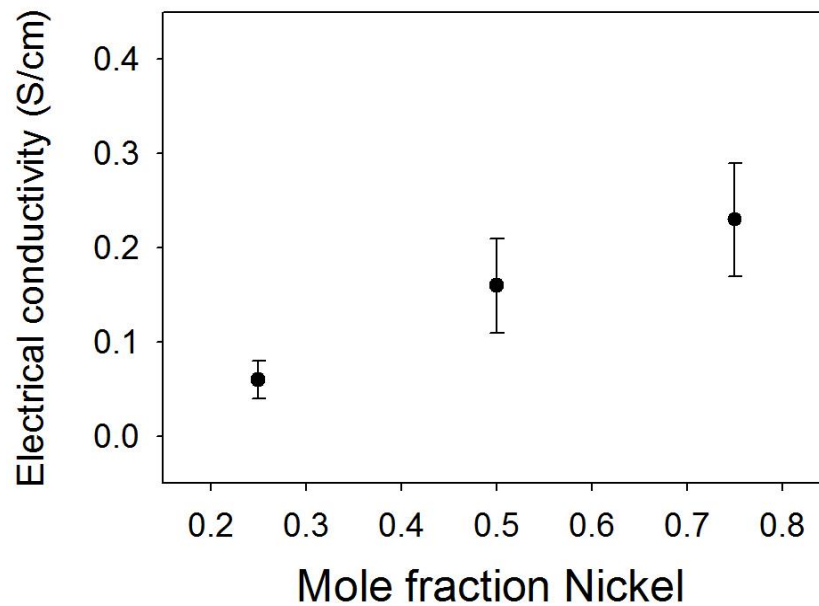
Figure S19. Enhancement in electronic conductivity of MMO thin films with varying nickel content in the composite determined using 4-point probe measurements

REFERENCES

1. R. Ding, L. Qi and H. Wang, *Electrochim. Acta*, 2013, **114**, 726-735.
2. F. C. Zheng, D. Q. Zhu and Q. W. Chen, *ACS Appl. Mater. Interfaces*, 2014, **6**, 9256-9264.
3. Z. Ren, V. Botu, S. B. Wang, Y. T. Meng, W. Q. Song, Y. B. Guo, R. Ramprasad, S. L. Suib and P. X. Gao, *Angew. Chem., Int. Ed.,* 2014, **53**, 7223-7227.
4. Y. Sharma, N. Sharma, G. V. S. Rao and B. V. R. Chowdari, *J. Mater. Chem.*, 2009, **19**, 5047-5054.
5. S. Mirhashemihaghighi, B. Leon, C. P. Vicente, J. L. Tirado, R. Stoyanova, M. Yoncheva, E. Zhecheva, R. S. Puche, E. M. Arroyo and J. R. de Paz, *Inorg. Chem.*, 2012, **51**, 5554-5560.
6. J. Q. Zhao and Y. Wang, *J. Mater. Chem. A*, 2014, **2**, 14947-14956.
7. M. J. Aragon, B. Leon, C. P. Vicente and J. L. Tirado, *J. Power Sources*, 2011, **196**, 2863-2866.
8. L. W. Su, Z. Zhou, X. Qin, Q. W. Tang, D. H. Wu and P. W. Shen, *Nano Energy*, 2013, **2**, 276-282.
9. M. M. Rahman, A. M. Glushenkov, T. Ramireddy and Y. Chen, *Chem. Commun.*, 2014, **50**, 5057-5060.